metals

Article

Beam Shaping in Laser Powder Bed Fusion: Péclet Number and Dynamic Simulation

Sergey N. Grigoriev, Andrey V. Gusarov, Alexander S. Metel, Tatiana V. Tarasova, Marina A. Volosova, Anna A. Okunkova * and Andrey S. Gusev

Department of High-Efficiency Processing Technologies, Moscow State University of Technology STANKIN, 127055 Moscow, Russia; s.grigoriev@stankin.ru (S.N.G.); a.gusarov@stankin.ru (A.V.G.); a.metel@stankin.ru (A.S.M.); tarasova952@mail.ru (T.V.T.); m.volosova@stankin.ru (M.A.V.); gusev.angrey@bk.ru (A.S.G.)

* Correspondence: a.okunkova@stankin.ru; Tel.: +7-909-913-12-07

Abstract: A uniform distribution of power density (energy flux) in a stationary laser beam leads to a decrease in the overheating of the material in the center of the laser beam spot during laser powder bed fusion and a decrease in material losses due to its thermal ablation and chemical decomposition. The profile of the uniform cylindrical (flat-top) distribution of the laser beam power density was compared to the classical Gaussian mode (TEM_{00}) and inverse Gaussian (donut) distribution (airy distribution of the first harmonic, $TEM_{01*} = TEM_{01} + TEM_{10}$). Calculation of the Péclet number, which is a similarity criterion characterizing the relationship between convective and molecular processes of heat transfer (convection to diffusion) in a material flow in the liquid phase, shows that the cylindrical (flat-top) distribution ($TEM_{01*} + TEM_{00}$ mode) is effective in a narrow temperature range. TEM_{00} shows the most effective result for a wide range of temperatures, and TEM_{01*} is an intermediate in which evaporation losses decrease by more than 2.5 times, and it increases the absolute laser bandwidth when the relative bandwidth decreases by 24%.

Keywords: energy excess; heat diffusion; laser beam mode; laser powder bed fusion; numerical simulation; profiling; power density distribution; thermal conductivity

Citation: Grigoriev, S.N.; Gusarov, A.V.; Metel, A.S.; Tarasova, T.V.; Volosova, M.A.; Okunkova, A.A.; Gusev, A.S. Beam Shaping in Laser Powder Bed Fusion: Péclet Number and Dynamic Simulation. *Metals* **2022**, *12*, 722. https://doi.org/10.3390/met12050722

Academic Editors: Antonio Riveiro and Matteo Benedetti

Received: 1 March 2022
Accepted: 18 April 2022
Published: 24 April 2022

1. Introduction

The well-known drawback of some laser material-processing technologies is non-uniform thermal conditions in the spot. The material is overheated in the center of the laser spot when an excess of the energy leads to intensive material evaporations and chemical decompositions [1–4], which is not characteristic of other additive technologies using alternative sources of concentrated energy flow [5,6]. Inversely, the material does not attain the necessary processing temperature at the periphery of the spot, and the energy is essentially lost by heat diffusion in the treated body (the target) [7–9]. Modern optics proposes shaping a laser beam that provides alternative laser power density distributions of transverse electromagnetic (TEM) mode:

- Airy distribution of the first harmonic (donut) $TEM_{01*} = TEM_{01} + TEM_{10}$;
- Uniform cylindrical (flat-top) distribution $TEM_{FT} = TEM_{01*} + TEM_{00}$.

These technical solutions have multiple laser powder bed fusion attempts but have never been researched theoretically with correction to the beam motion [10–12].

The lack of a reliable solution in terms of heat redistribution leads to the following disadvantages affecting the quality of parts obtained by laser-additive manufacturing and processing productivity (Figure 1) [13–17]:

- Local overheating, capturing the underlying layers, creating additional stresses during metal solidification (partially solved by subsequent heat treatment and preliminary heating of the substrate) [18–20];

- Active evaporation of the material and its chemical interaction with the atmosphere of the chamber (reduced due to the use of more gentle processing modes, which dramatically affects productivity) [21–23];
- Ejecting material from the processing area (reduces the surface quality of the part itself, damages the optics, and is reduced by gentle modes and preheating of the platform) [24–26].

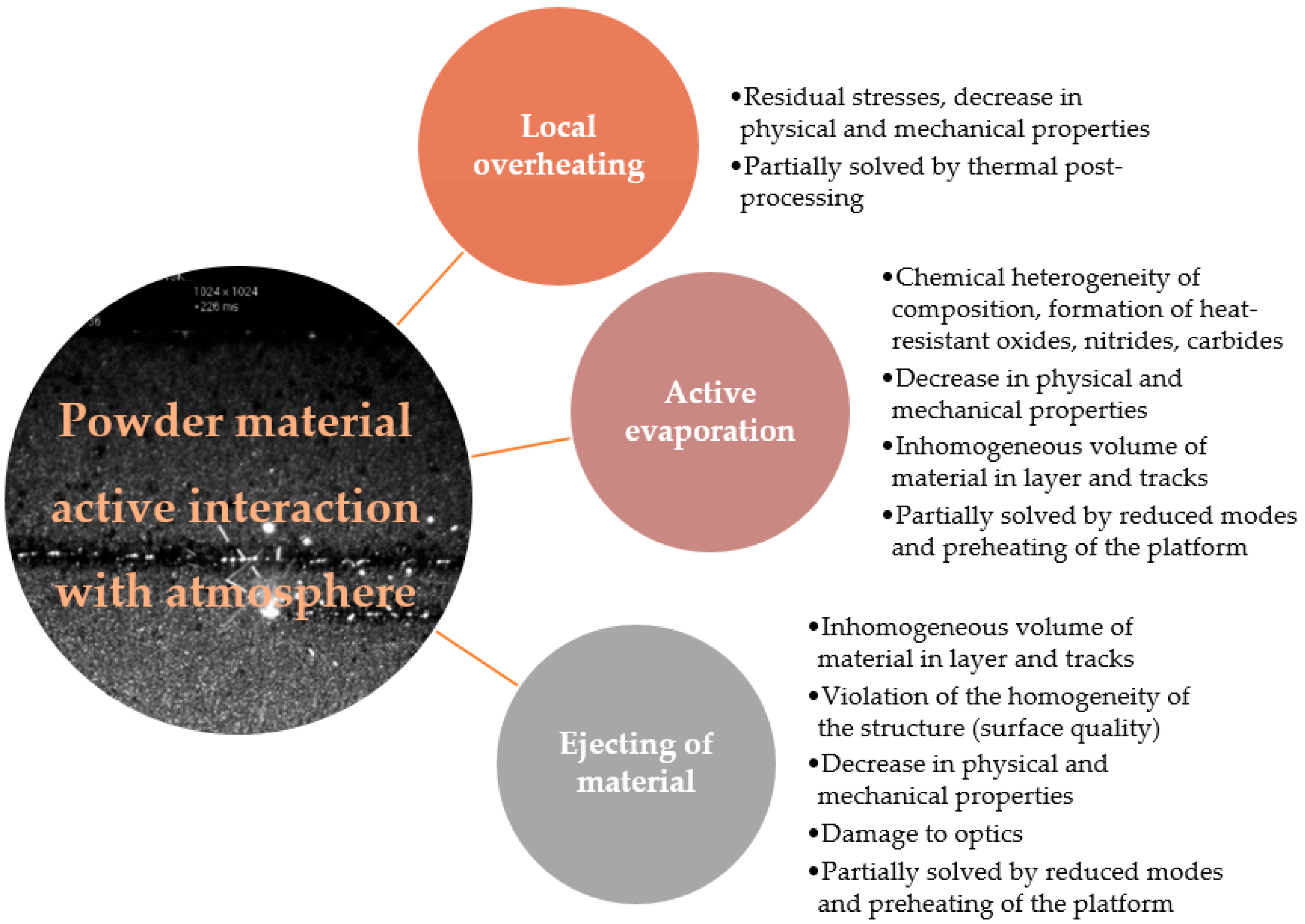

Figure 1. The main consequences of the active interaction of powder material with atmosphere and the existing ways of solving them.

An obvious disadvantage of using optical means for redistributing laser energy into the beam can be its expansion by 150–350%, which may not allow for obtaining more precision parts, but can become a significant advantage in the production of products with dimensions of more than 100 mm, for which the width of the heat-affected zone will be significantly reduced [27,28]. Figure 1 is based on the results of optical diagnostics and video monitoring described in detail in [27].

There are many factors that influence the final surface quality (roughness, uniformity, and dimensional accuracy) [29–33] such as:

- laser power, spot size, and laser power distribution among the laser system and optic parameters,
- scanning speed and strategy and hatch distance among strategy parameters,
- powder particle size, shape and morphology, and layer thickness among powder parameters,
- inertness of the atmosphere, impermeability of the chamber, dimensions of the part on the working platform (maximum angle of deviation of the beam from the vertical), and so on.

The conventional power (energy flux q, W/mm^2) density distribution in radius r of the laser focus is the classical bell-like one approximated by the normal Gauss distribution (Laguerre–Gaussian mode, circularly symmetric beam profile TEM_{00}) of the optical resonator as:

$$q = \frac{P}{\pi r_0^2} \exp\left(-\frac{r^2}{r_0^2}\right), \tag{1}$$

where P is the laser beam power, W and r_0 is the radius circle, mm.

In some laser-based technologies such as lithography (photo-activated processes) [34,35], laser scribing [36,37], and thin surface laser treatment (including medical purposes) [38–41], the optimal beam profile seems to be the flat-top (TEM_{FT}) one that provides the energy flux's uniformity (uniform laser power density distribution). The typical powder consolidation mechanisms in laser powder bed fusion are thermo-activated [42]. Then the objective is transferred from the uniform power density distribution (energy flux q, W/mm^2) to a radiation-induced uniform temperature field T (°C).

Since the thermal energy is released on an adiabatic plane bounding a uniform conducting half-space inside a circle of radius r_0 (mm), with radial distribution [43]:

$$q = \frac{P}{2\pi r_0^2} \frac{1}{\sqrt{1 - r^2/r_0^2}}, \tag{2}$$

the temperature rise over the circle:

$$T_0 = \frac{P}{4\lambda r_0}, \tag{3}$$

where λ is the material thermal conductivity, W/mm·K. In this case, the laser radiation is absorbed by layered powder to heat a massive body with conduction as the principal heat transfer mechanism. Then profile (2) can be better for laser powder bed fusion and similar laser-based powder technologies. TEM_{FT} profile (the cylindrical flat-top temperature distribution) is challenging to obtain because of a discontinuity at the beam boundary where $r = r_0$. Then the airy distribution of the first harmonic, (donut of the first overtone) TEM_{01*}, seems to be a reasonable compromise [43]:

$$q = \frac{P}{\pi r_0^2} \frac{r^2}{r_0^2} \exp\left(-\frac{r^2}{r_0^2}\right), \tag{4}$$

In the thermo-activated processes, the laser beam scans the powder surface, resulting in a non-uniform temperature distribution over the laser spot for various laser beam profiles [44,45]. An inverse problem of heat diffusion for the scanning laser beam can be solved to find the ideal power density distribution. Still, the solution mainly depends on the scanning speed factor—its value and direction. The influence of direction on the absorbed energy flux shows that the laser beam profile would be asymmetric. Moreover, the laser beam scans quite fast (up to 400 mm/s) and changes direction rapidly. Therefore, it can be an even more complicated scientific and technical task never solved before, since most of the published work on beam profiling considers the symmetric beam for their calculations.

This work aims to compare three types of abovementioned laser beam profiles, research the influence of the scanning speed in a linear medium, and develop a non-linear model, including the material evaporation factor.

2. Numerical Simulations

2.1. Simulations and Influence of Scanning Speed

The powder layer on the target surface is considered thermally thin and is not taken into account. Laser radiation is supposed to be absorbed on the surface. In the case of partial reflection, the laser power in the equations mentioned above means the absorbed part of the laser beam radiation. In the coordinate system moving with the scanning speed, the steady-state heat diffusion equation is [43]:

$$\alpha \Delta T + u_s \frac{\partial T}{\partial x} = 0, \tag{5}$$

where u_s is scanning speed, m/s; α is the thermal diffusivity, m^2/s; and Δ is the Laplace operator. Equation (5) is solved by numerical or analytical methods where possible, with boundary condition:

$$T \to T_a \text{ at } x \to \pm\infty,\ y \to \pm\infty,\ z \to \infty, \tag{6}$$

where T_a is the ambient temperature. The target surface z = 0 is adiabatic, excluding the laser spot where

$$-\lambda \frac{\partial T}{\partial z} = q. \tag{7}$$

The temperature fields are presented in Figures 2 and 3.

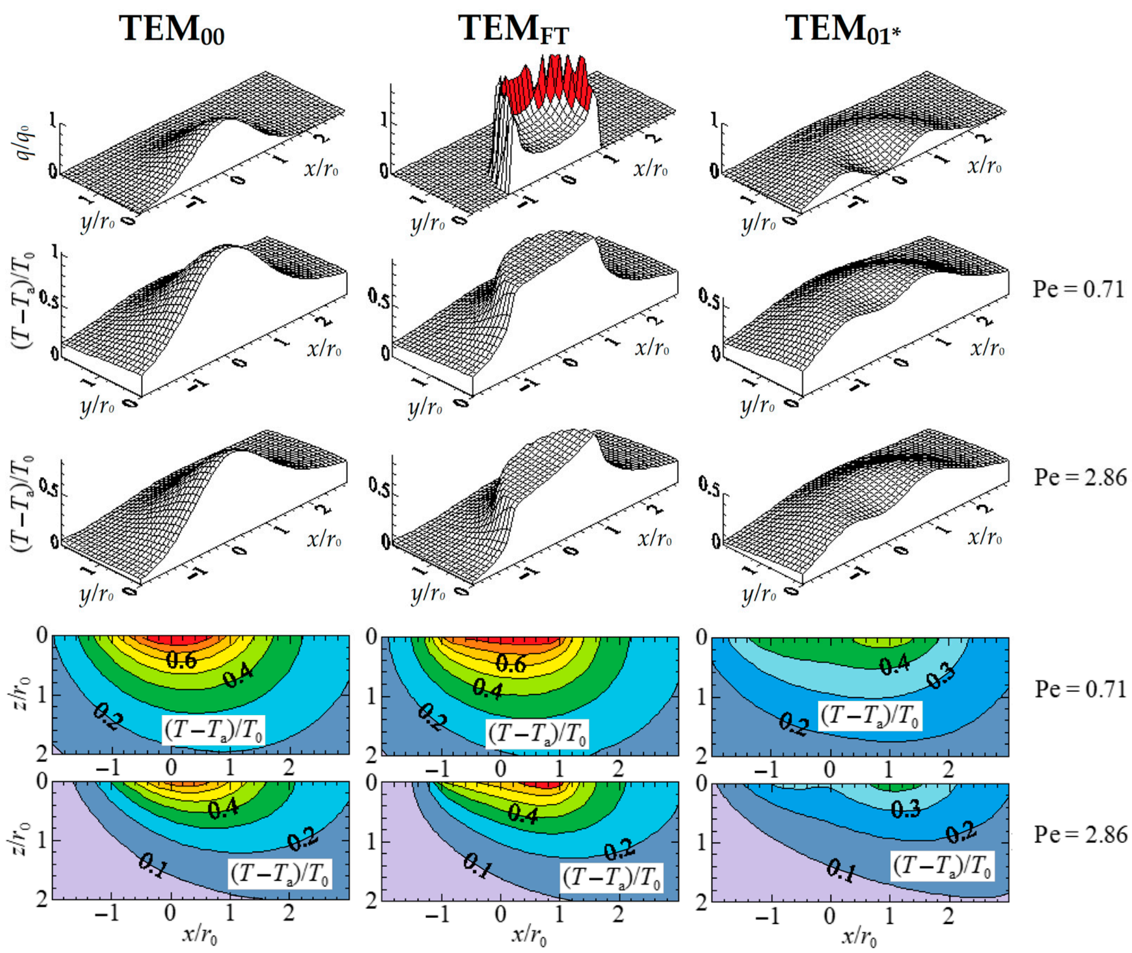

Figure 2. Normalized distributions: flux density of the absorbed laser energy q over the target surface z = 0 (top row); temperature T over the target surface (second and third rows); temperature T over the vertical plane of mirror symmetry y = 0 formed by the beam axis and the scanning line (two rows on the bottom). Red in the q/q_0 graph indicates the approach to the area of the discontinuity at the beam boundary where $r = r_0$.

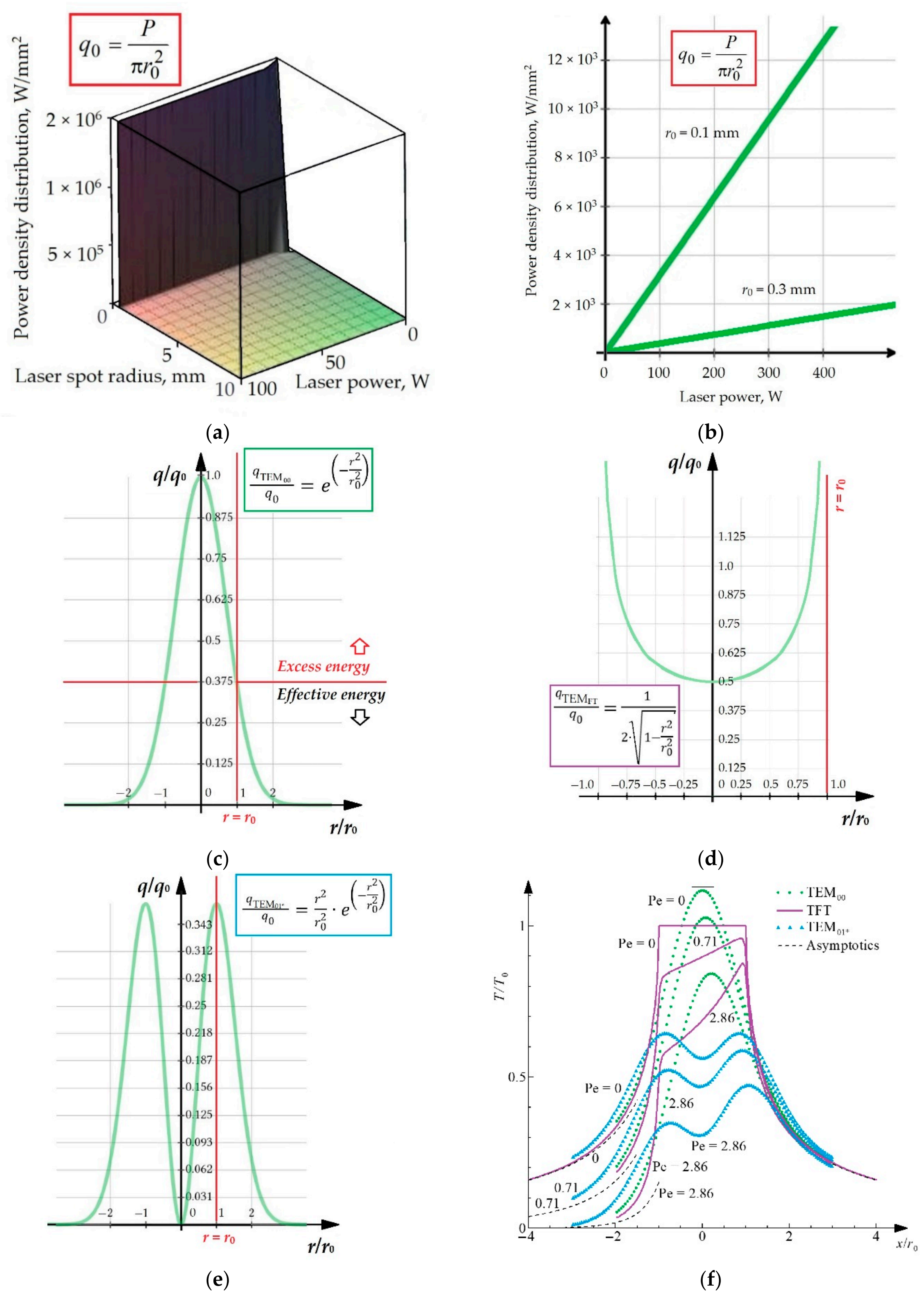

Figure 3. 3D plot of the implicit function q_0 (**a**); implicit function q_0 for various values of r_0 (**b**); normalized implicit function q/q_0 (TEM_{00} profile) (**c**); normalized implicit function q/q_0 (TEM_{FT} profile) (**d**); normalized implicit function q/q_0 (TEM_{01^*} profile) (**e**); and temperature distributions along the direction of the scanning speed on the surface, when $y = 0$, $z = 0$ (**f**). The beam boundary where $r = r_0$ is marked red in graphs (**c**–**e**).

The scanning speed is specified by the thermal Péclet number:

$$\mathrm{Pe} = \frac{2r_0 u_s}{\alpha}. \tag{8}$$

The temperature rise relative to the ambience ($T - T_\mathrm{a}$) is normalized by T_0 specified by Equation (3). Normalizing coordinates by r_0 makes the obtained results universal for a linear conductive medium. The results significantly depend on the Péclet number. The top row in Figure 2 shows two-dimensional views of laser profiles (1), (2), and (4) normalized by [43] (Figure 3a,b):

$$q_0 = \frac{P}{\pi r_0^2}. \tag{9}$$

The normalized graphs of profiles are as follows (Figure 3c–e):

$$\frac{q_{\mathrm{TEM}_{00}}}{q_0} = e^{\left(-\frac{r^2}{r_0^2}\right)}, \tag{10}$$

$$\frac{q_{\mathrm{TEM}_{\mathrm{FT}}}}{q_0} = \frac{1}{2\cdot\sqrt{1-\frac{r^2}{r_0^2}}}, \tag{11}$$

$$\frac{q_{\mathrm{TEM}_{01*}}}{q_0} = \frac{r^2}{r_0^2}\cdot e^{\left(-\frac{r^2}{r_0^2}\right)}. \tag{12}$$

The other rows in Figure 2 are two-dimensional temperature distributions over two characteristic planes. The 3D plot of the implicit function is shown in Figure 3a.

Figure 3f shows all the obtained results as profiles of the surface temperature along line $y = 0$, $z = 0$. For all laser profiles, the temperature profiles decrease with the increase of Pe that corresponds to the increase of the scanning speed. The forward temperature front becomes sharper with the increase of Pe, and the backward temperature front is insensible to Pe, according to the well-known asymptotics:

$$\frac{T-T_a}{T_0} = \frac{2}{\pi}\frac{r_0}{R}\exp\left(\frac{\mathrm{Pe}}{4}\frac{x-R}{r_0}\right), \tag{13}$$

with $R^2 = x^2 + y^2 + z^2$, shown by dashed lines in Figure 3f. In the case of mode TEM_{00}, all three numerically calculated temperature profiles are bell-like. At Pe = 0, the maximum is in the origin. The numerically obtained maximum value is about the analytical result $T_{\max}$,

$$\frac{T_{\max}-T_a}{T_0} = \frac{2}{\sqrt{\pi}}, \tag{14}$$

shown by a horizontal dash in Figure 3f. The increase of Pe slightly shifts the position of the temperature maximum in the direction opposite to that of the scanning speed vector that is explained by the thermal inertia of the target.

At Pe = 0, the flat-top laser beam profile forms steady-state temperature distribution

$$\frac{T-T_a}{T_0} = \frac{2}{\pi}\arcsin\frac{2r_0}{\sqrt{(r-r_0)^2+z^2}+\sqrt{(r+r_0)^2+z^2}}, \tag{15}$$

where $r^2 = x^2 + y^2$, with an exactly horizontal plate over the laser spot. When Pe increases, this plate inclines towards the scanning speed vector and slightly sags. In the case of donut mode, the surface temperature distribution inherits the ring-like ridge. The ridge becomes more asymmetric with the increase of Pe (Figure 3f).

2.2. Temperature and Energy Flux Profiles

Temperature distribution in a cross-section perpendicular to the scanning direction cannot objectively characterize the temperature conditions for laser powder bed fusion because retarding the maximum target temperature relative to the central cross-section $x = 0$. The retardation depends on the scanning speed value and the distance from the scanning axis (X). The most representative quantity is the maximum temperature along axis X for threshold-like and Arrhenius temperature dependencies of the process kinetics. Figure 4a shows the transverse profile of the quantity on the surface [43]:

$$\max_x T(x, y, 0), \tag{16}$$

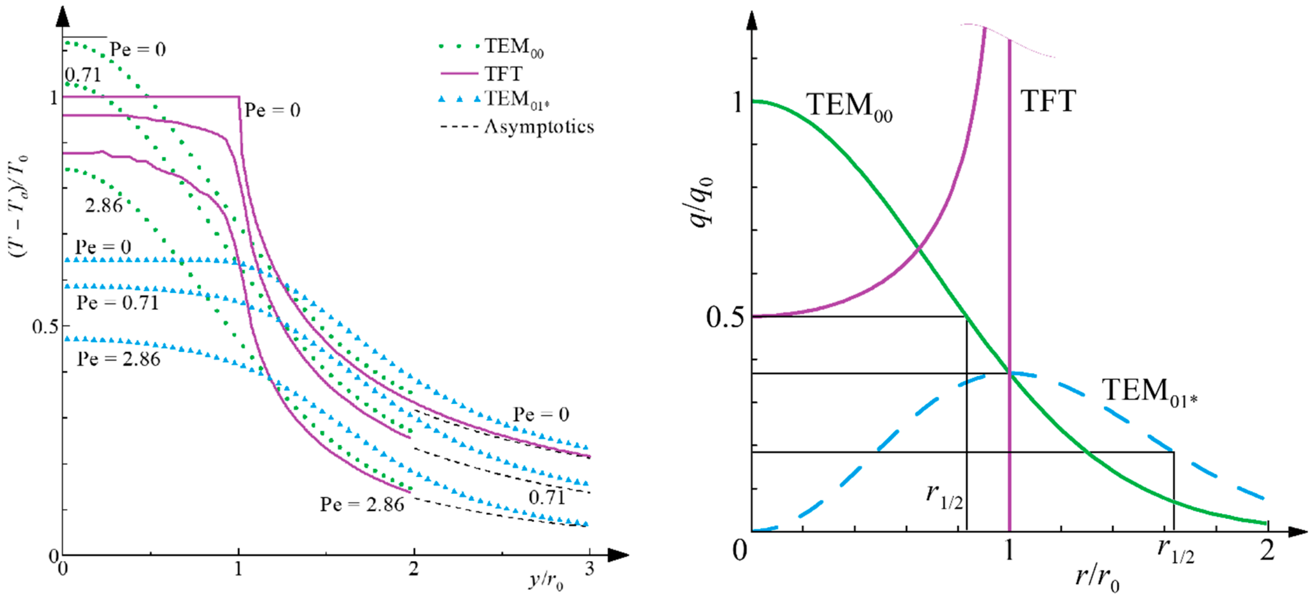

(**a**) (**b**)

Figure 4. Maximum temperature T on the target surface $z = 0$ versus distance y from the scanning axis (**a**); the testing profiles (q/q_0) and estimation of their radii at half-width $r_{1/2}$ (**b**).

The asymptotics at Pe = 0 are given by Equation (13) at $x = 0$. At Pe = 0.71 and Pe = 2.86, the asymptotics are obtained by numerical treatment of Equation (13) by Equation (16). The widths of the re-melted zone on the surface often estimate the contact's width between the consolidated powder, and the substrate can be deduced by this profile.

The transverse profiles of the surface temperature shown in Figure 4a present the thermal conditions for laser powder bed fusion. They cannot be compared with the tested laser beam profiles because all the obtained temperature profiles have different absolute maxima. The tentative laser-beam radius r_0 is not an objective measure of its width applicable to various beams' radial profiles. Thus, beam TEM_{01*} in Figure 4b seems wider than beam TEM_{00} at the same r_0. Let us estimate the width of a laser profile by its diameter at half-maximum $d_{\frac{1}{2}}$ that is conventional in laser technology applications. The scheme for estimating the corresponding radius at half-maximum $r_{\frac{1}{2}} = d_{\frac{1}{2}}/2$ is shown in Figure 4b and Table 1.

Table 1. Calculated absolute maximum of temperature T_{max} versus Péclet's number Pe.

Laser Beam Profile	Beam Radius at Half Maximum, $r_{1/2}/r_0$	$(T_{max} - T_a)/T_0$		
		Pe = 0	Pe = 0.71	Pe = 2.86
TEM_{00} (Gaussian)	$\sqrt{\ln 2} = 0.8326$	$2/\sqrt{\pi} = 1.128$	1.027	0.8417
TEM_{01^*} (donut)	1.6366	1.6453	0.5889	0.4735
TEM_{FT} (flat-top)	1	1	0.9613	0.8819

It should be noted that temperatures above T_{max} are unallowable because of material evaporation or chemical decomposition. Temperatures below the minimum T_{min} are not sufficient to complete the specified physical or chemical processes. The boiling point is specified as T_{max}, and the melting point is T_{min} for laser powder bed fusion of pure metals [46,47]. For alloys, T_{max} and T_{min} are determined by the component with the lowest boiling and melting points, correspondingly.

The temperature dependencies of the kinetic constants can be taken into account to define the laser powder bed fusion interval (T_{min}, T_{max}). The maximum temperature in the laser-processing zone and the width of the laser beam characterized by $d_{1/2}$ or $r_{1/2}$ can be effectively controlled by variation of the laser power or by laser beam expansion. The former quantity can be set at T_{max}. The latter quantity can be set at the specified dimensional uncertainty.

Figure 5 shows the same temperature profiles as in Figure 4a to apply the chosen criterion for evaluating the laser beam profiles. However, these profiles are renormalized by their absolute maxima, height, laser beam radii at half maximum, and width. The normalizing constants for all the nine testing profiles are obtained from the data shown in Figure 4a,b and Table 1. A qualitative review of the temperature profiles shown in Figure 5 indicates that laser profile TEM_{FT} results in the broadest top of the temperature profile, as expected. Laser profile TEM_{00} results in the broadest base of the temperature profile. This means that evaluating the three tested laser profiles is not straightforward and depends on the acceptable temperature range of laser treatment $T_{max} - T_{min}$ relative to the maximum temperature increment $T_{max} - T_a$. If the acceptable temperature range is narrow, the treated band of the surface is near the top level of the temperature profile. In this case, theoretically, the flat-top profile provides the widest laser-treated band, which means the most effective use of the laser energy. If the acceptable temperature range is wide, the most effective profile seems to be TEM_{00}.

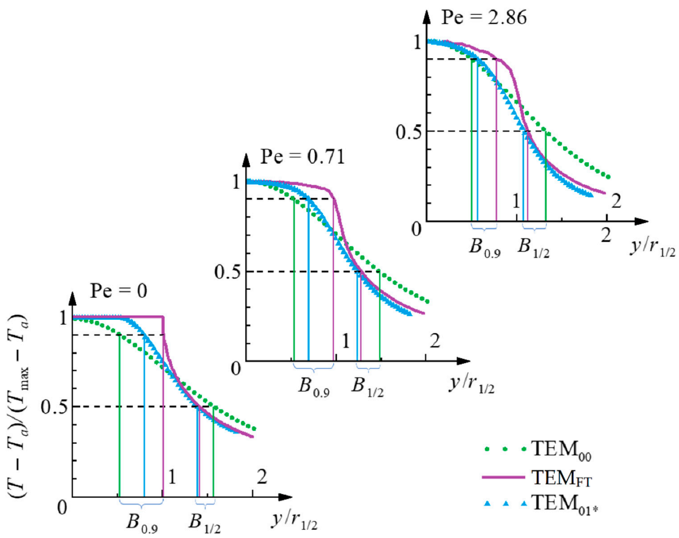

Figure 5. Normalized transverse profiles of the maximum surface temperature and the definition of the widths of laser-treated band ($B_{1/2}$ and $B_{0.9}$).

3. Model Evaluation

3.1. Quantitative Evaluation

Let us introduce the width of the laser-treated band B_n where non-dimensional parameter γ for quantitative evaluation of the laser beam profile characterizes the relative temperature range of the laser treatment [43]:

$$\gamma = \frac{T_{min} - T_a}{T_{max} - T_a}. \quad (17)$$

The definitions of $B_{1/2}$ and $B_{0.9}$ are shown in Figure 5. Band $B_{1/2}$ approximately corresponds to laser powder bed fusion of metals and alloys such as CoCr at the ambient temperature T_a with T_{max} equal to the boiling/decomposition point (~2800–3300 °C) and T_{min} equal to the melting point (~1250–1650 °C) [48]:

$$\gamma_{CoCr} = \frac{1458\ °C - 20\ °C}{3000\ °C - 20\ °C} \approx 0.4826. \quad (18)$$

The main properties of the cobalt-chromium alloy are shown in Table 2. The data presented in the table are taken from [49,50].

Table 2. Properties of the cobalt-chromium alloy (64–65% of Co, 29–30% of Cr).

Properties	**Density, g/cm^3**	**Melting Point, °C**	**Boiling Point, °C**	**Tensile Strength, kN/cm^2**	**Yield Strength, kN/cm^2**	**Young's Modulus, GPa**	**Coefficient of Thermal Expansion, $\times10^{-6}$ °C^{-1}**	**Thermal Conductivity, W/(m·K)**
CoCr alloy	8.0–8.4	1250–1650	2800–3000	≥61.7–70	≥50–64	210–250	11.2–14.2	13

Band $B_{0.9}$ corresponds to laser-additive manufacturing of oxide ceramics at the ambient temperature T_a with T_{max} equal to the temperature of chemical decomposition (~2900 °C) [51–55]. T_{min} should be chosen as high as possible because of the Arrhenius temperature dependence of the powder consolidation rate [56].

The calculated values of $B_{1/2}$ and $B_{0.9}$ versus Péclet's number for the laser beam profiles are shown in Table 3 and Figure 6. In the considered range of Péclet's numbers (Pe = 0–2.86), the conventional Gaussian profile of TEM_{00} seems to be the most effective for the wide temperature range of laser treatment of $\frac{1}{2}$ (alloys, metals) when the flat-top profile can be significantly more advantageous for the narrow temperature range of 0.9 (mostly oxide ceramics). For $B_{1/2}$, profile TEM_{01*} seems to be the least effective one, and the flat-top is intermediate. For $B_{0.9}$, profile TEM_{00} seems to be the least effective one, and TEM_{01*} is intermediate.

Table 3. Calculated widths of the laser-treated band $B_{1/2}$ and $B_{0.9}$ versus Péclet's number.

Laser Beam Profile	**$B_{1/2}/d_{1/2}$**			**$B_{0.9}/d_{1/2}$**		
	Pe = 0	**Pe = 0.71**	**Pe = 2.86**	**Pe = 0**	**Pe = 0.71**	**Pe = 2.86**
TEM_{00} (Gaussian)	1.57	1.485	1.32	0.53	0.535	0.50
TEM_{FT} (flat-top)	1.415	1.28	1.118	1.012	0.974	0.775
TEM_{01*} (donut)	1.39	1.24	1.07	0.80	0.70	0.565

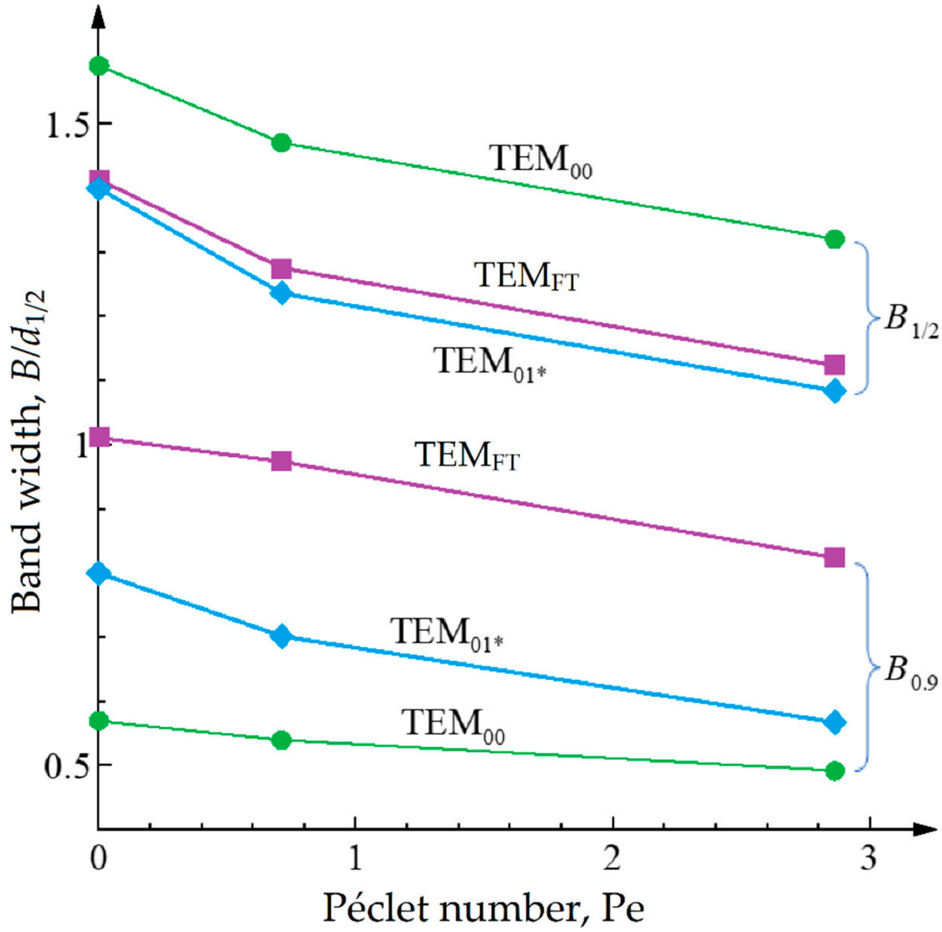

Figure 6. Widths of the laser treated band $B_{1/2}$ and $B_{0.9}$ versus Péclet's number.

3.2. Dynamic Evaluation

Let us calculate the steady temperature at the laser spot boundary for two laser modes and a laser power of 100 and 400 W. The experimental diameter of the laser spot will be approximately 100 μm (0.001 m) for the TEM_{00} mode and 300 μm (0.003 m) for the TEM_{01*} mode (Table 4) [57]. As can be seen, with an increase in the power of laser radiation to 400 W, due to excess heat, a multifaceted local overheating is predicted (the calculated temperature is 2.56 times higher than T_{max}) at the boundary of the laser radiation of the Gaussian mode (as a result, active evaporation of metal from the processing zone). At the same time, when using the reverse Gaussian profile (donut), the temperature at the edge of the laser spot does not reach T_{min} (less than 2.34 times), which means that there is no sufficient heat to initiate the CoCr alloy granule fusion. The powder consolidation temperature can be closer to the melting temperature. Implicit graphs of the function of temperature on the radius for a cobalt-chromium alloy (λ = 13 W/(m·K)) depending on the power of laser radiation are shown in Figure 7 (Equation (3)). It should be noted that Figure 7a is an implicit graph of the temperature ($T_{max} - T_a$) on the radius and laser power function for the material with the mentioned material thermal conductivity, where the solution area is marked red, since only values above zero can be taken into account for technological purposes, since other areas have no physical sense in the context of engineering.

Table 4. The steady temperature values at the laser spot boundary for two laser modes.

Laser Beam Profiles	Laser Spot Diameter, mm	Steady Temperature ($T_{max} - T_a$), K	
		P = 100 W	P = 400 W
TEM_{00} (Gaussian)	~0.1	1923	7692
TEM_{01^*} (donut)	~0.3	641.03	2564

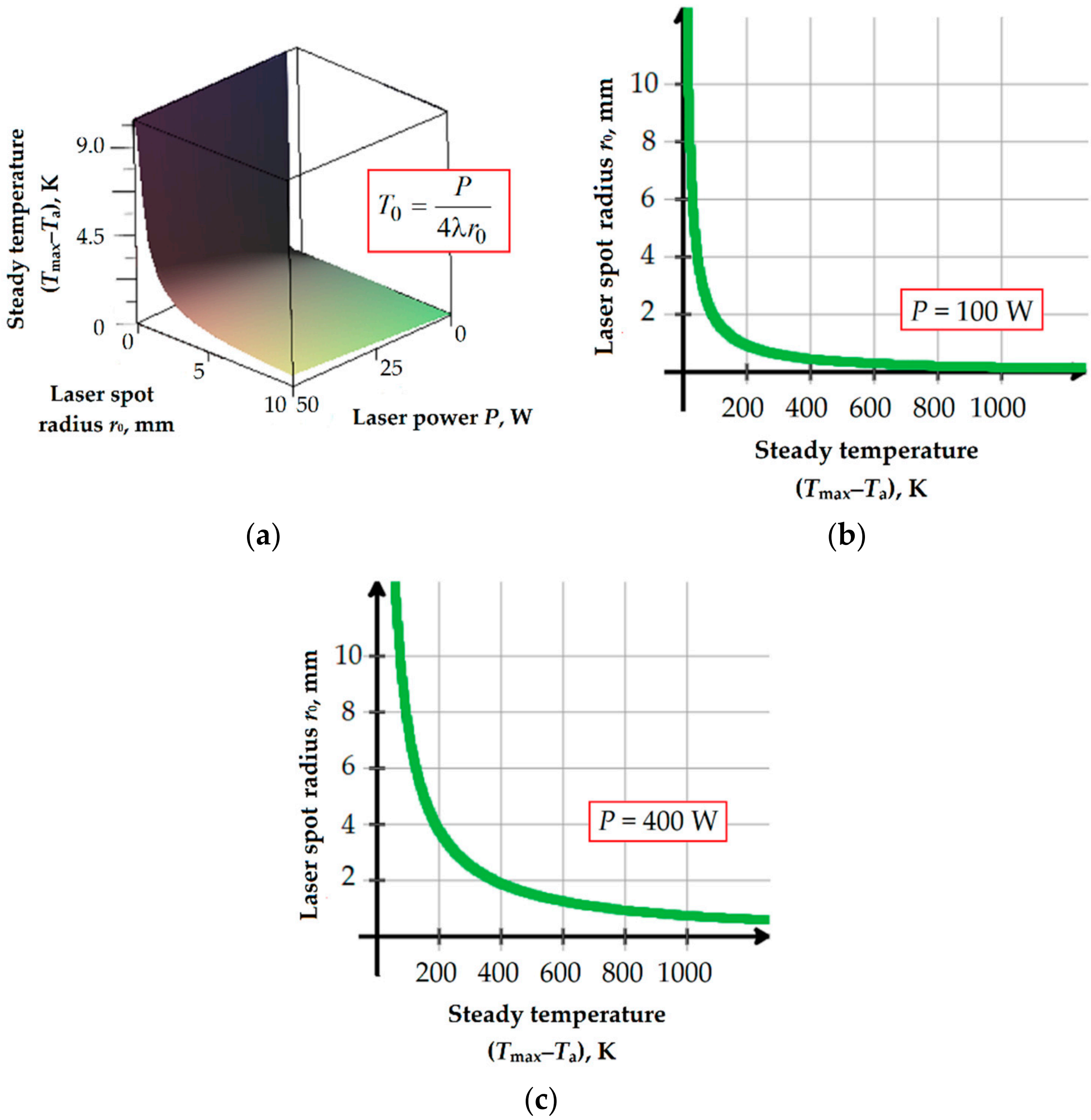

Figure 7. Implicit graphs of the function of temperature ($T_{max} - T_a$) on the radius depending on the power of laser radiation for λ = 13 W/(m·K): (**a**) 3D-plot; (**b**) P = 100 W; (**c**) P = 400 W.

Table 5 presents two evaluated groups of laser beam parameters based on the experimental data obtained by optical achievements of the laser beam profiles using an expander and profiler installed in the LPBF setup and optical evaluation of the obtained profiles [28]. Specific energy contribution (J/m^2) was calculated by:

$$E = \frac{q_0}{u_s}. \tag{19}$$

Table 5. Parameters of laser powder bed fusion chosen for modeling.

Factor	Measuring Unit	Values	
Absorbed power of the beam, P	W	100	400
Laser beam radius, r_0	mm	~0.1/2	~0.3/2
Scanning velocity, u_s	m/s	0.0213	0.0286
Normalized power density distribution, q_0	W/m^2	0.320×10^8	0.142×10^8
Specific energy contribution, E	J/m^2	1.5×10^5	0.5×10^5
Péclet's number, Pe	-	0.71	2.86

Two numerical calculations for Gaussian (Equation (1)) and donut (Equation (4)) laser beam profiles are made for each group. Thermal diffusivity of CoCr alloy is presented in Table 6 [58,59]:

$$\alpha = \frac{\lambda}{\rho \cdot C_p}, \tag{20}$$

where ρ is density, kg/m^3 and C_p is specific heat capacity, J/(kg·K). The dependence of the Péclet number on the laser spot radius and scanning speed for a cobalt-chromium alloy is shown in Figure 8.

Table 6. Thermal diffusivity α of CoCr alloy.

Thermal Diffusivity α, cm^2/s	
at 20 °C	at 500 °C
0.02–0.14	0.03–0.074

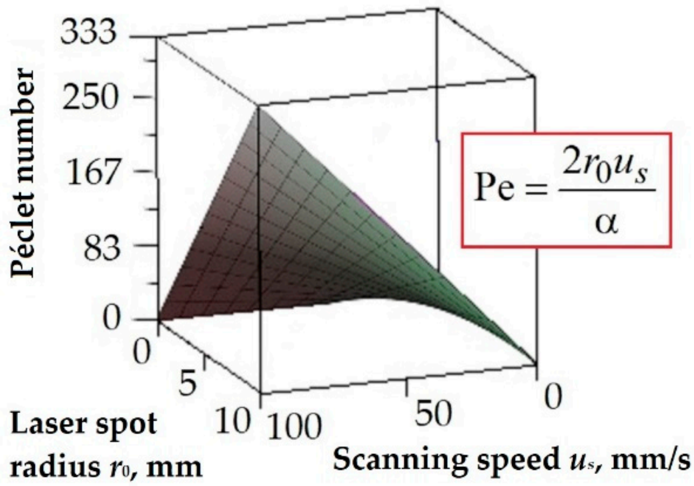

Figure 8. The implicit graph of the Péclet number on the laser spot radius and scanning speed for a cobalt-chromium alloy (α = 5.2 × 10^{-6} m^2/s) (3D-plot).

Figure 9 shows the calculated temperature fields for two types of laser beam profiles: TEM_{00} and TEM_{01*} at laser powers of 100 and 400 W, correspondingly, when laser beam diameters are 0.109 and 0.310 mm, respectively. The difference from Figure 2 is that laser beam profiles are shown at the level of calculated steady temperatures (Table 4). Formation of the temperature plateau is explained by a small value of overheating sufficient for evaporation under the given conditions. In the case of mode TEM_{01*}, the characteristic temperature sink is still visible in the center. The energy losses for evaporation are listed in Table 7. The corresponding mass losses are proportional to the energy ones [43]. Comparison of values listed in Table 7 indicates that the change from mode TEM_{00} to mode TEM_{01*} decreases the evaporation loss for all four calculations made. Thus, the laser profile corresponding to mode TEM_{01*} seems to provide more efficient laser power density distribution (Figure 10).

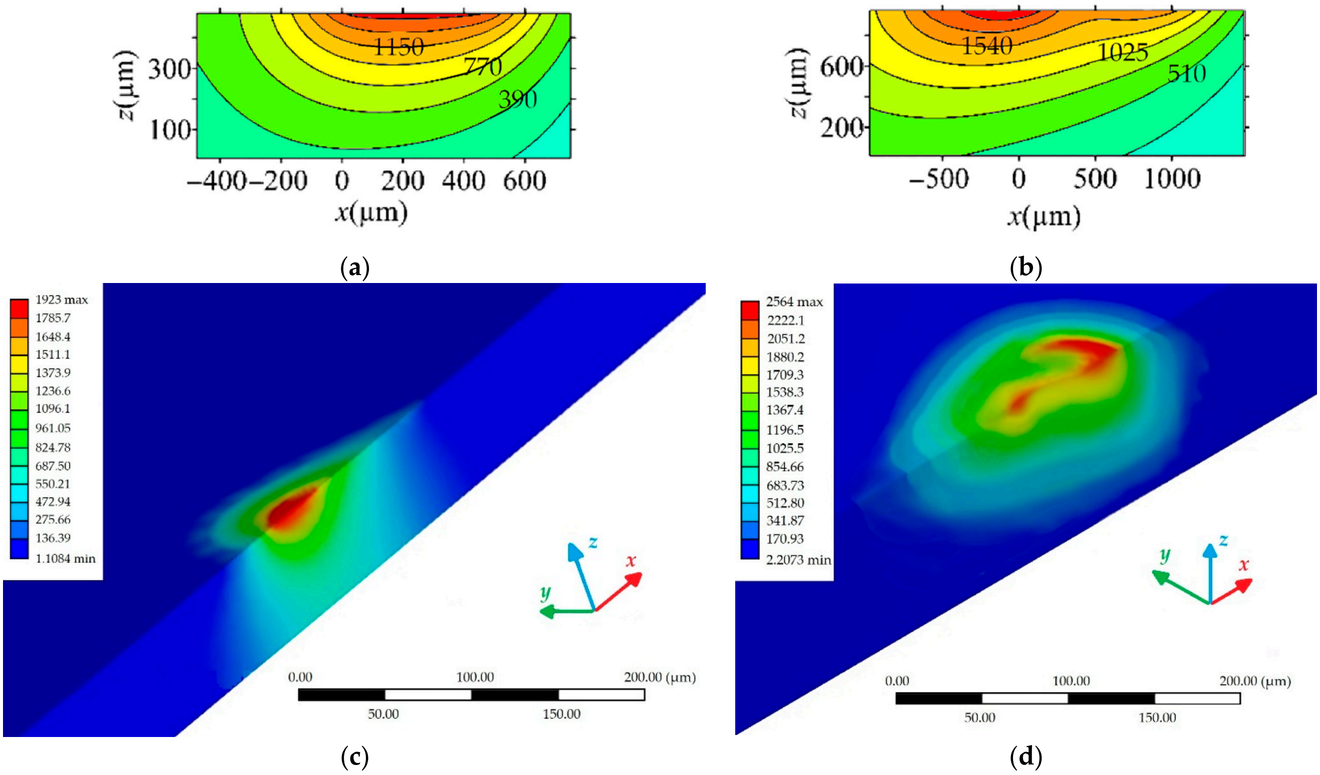

Figure 9. Calculated temperature distributions ($T_{max} - T_a$) in CoCr alloy: (**a**) over the vertical plane of mirror symmetry $y = 0$ formed by the beam axis and the scanning line for P = 100 W, Pe = 0.71; (**b**) over the vertical plane of mirror symmetry $y = 0$ formed by the beam axis and the scanning line for P = 400 W, Pe = 2.86; (**c**) results of temperature fields modeling for P = 100 W, Pe = 0.71 (cross-section); (**d**) results of temperature field modeling for P = 400 W, Pe = 2.86 (cross-section).

Table 7. Calculated values of power loss for evaporation P_v for CoCr alloy for the laser beam profiles.

Parameter	**Evaporation Loss, P_v (W)**	
	TEM_{00}, P = 100 W, Pe = 0.71	**TEM_{01^*}, P = 400 W, Pe = 2.86**
Max vapor velocity u_v, m/s	3.63	14.51
Max recoil pressure $p_{recoil} - p_0$, Pa	17.67	267.67
Mass loss rate L_{mass}, mg/s	144.30	520.22
Recoil force F_{recoil}, mN	0.55	7.57
Power loss for evaporation P_e, W	3.53	2.68

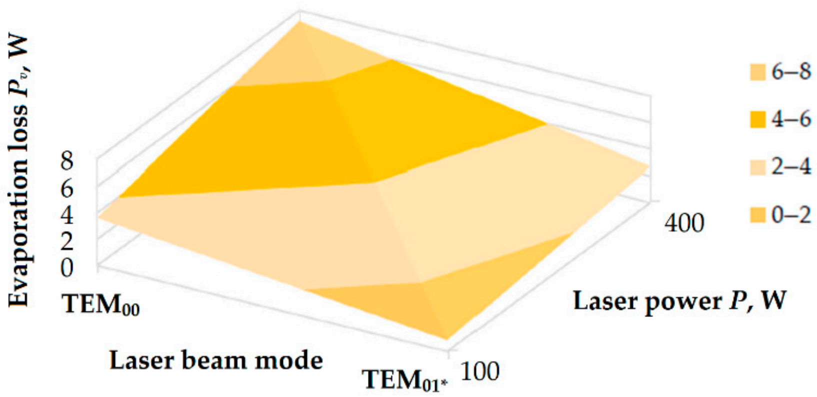

Figure 10. Calculated graphical presentation of power loss for evaporation P_v.

4. Discussion

It should be noted that the proposed dynamic model could not be used for precise data on the thermal history and simulation of the thermal stresses. The point was in researching an optimal laser power density distribution for the engineering tasks of LPBF. As known, the optimal melt pool configuration for the tasks of thick (more than 10 mm in thickness) material laser cutting or welding is torch-like (Figure 11) [25] and has a certain disadvantage when the laser power exceeds 100 W [26]. For laser scribing, surface treatment, and LPBF [40,41], the optimal one can be a more surface-like uniform distribution related to the following issues [60]:

a. avoiding overheating in the centrum of the melt pool and consequences such as material loss on evaporation and ejecting granules from the melt pool of thermal heat with the laser power set at more than 100 W;
b. avoiding secondary remelting and involvement of the previously solidified layers in the newly formed melt pool; and
c. melt ejection under steam pressure.

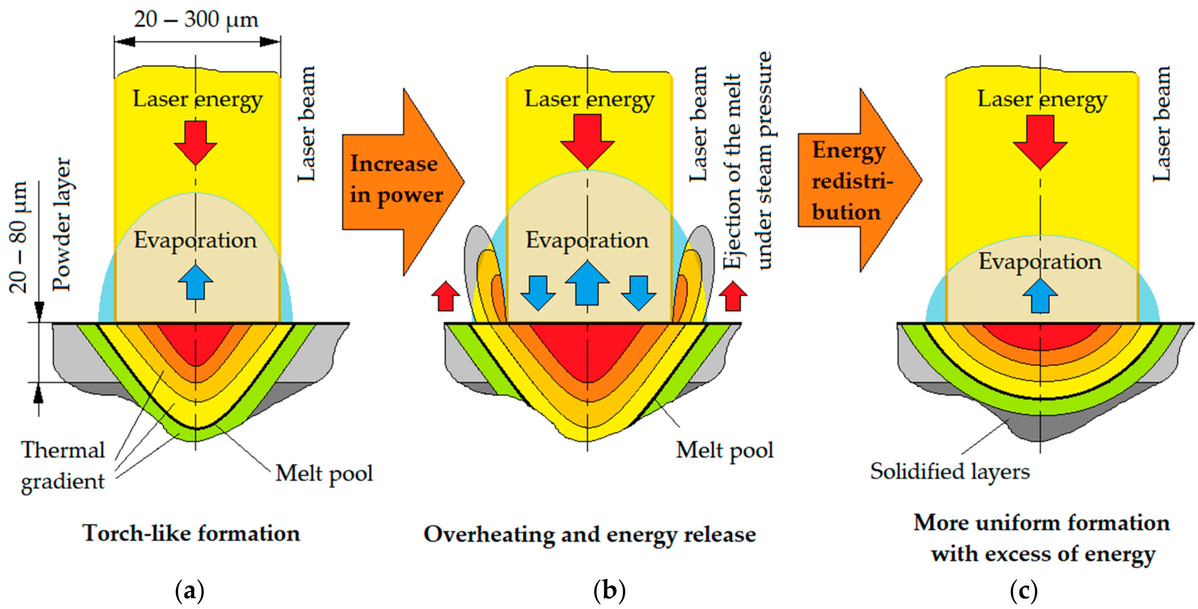

Figure 11. Melt pool formation: (**a**) torch-like; (**b**) torch-like with an increase of energy in the laser beam; (**c**) more uniform surface-like with an increase of redistributed energy in the melt pool.

The conducted research confirmed the effectiveness of the proposed approach not only for static modeling but for a dynamic one, as well. Achieved laser beam profiles are presented in Figure 12. As can be seen (Figure 12c), the flat-top profile is practically hard to be achieved close to the theoretical profile using the existed optical means [60]. The provided Figure 12d–f are reconstructed from the formed CoCr single tracks (Figure 12g–i) [61,62]. A detailed description of the developed LPBF setup equipped with an optical laser beam profiler and expander and optical diagnostics are presented in [26]. The experimental conditions are presented in [57]. Figure 13 presents the optical and modulation systems of LPBF setup.

The dynamic melt pool evaluation during experiments with metallic powders by optical diagnostic means [63,64] is expected for further research.

It should be noted that TEM_{FT} cannot be called a "desirable intensity distribution" since it was a theoretical proposal [50]. The idea was to achieve a more uniform energy density instead of peaks in the centrum of the laser beam spot. The picture of energy distribution in the laser beam spot and adsorbed energy by powder material is different. However, it can be even more varied, considering the dynamic factor (Pe number). Desirability can only be called a distribution that allows the achievement of uniform energy adsorption in the laser beam spot [57], taking into account the used material's thermal conductivity and dynamic factor. Definitely, it will be already varied for metallic [65,66] and ceramic [67–69] groups of materials. However, it can also vary depending on granulomorphometric parameters of the powder, mainly shape and reflect ability [45,70,71], which was not considered in the article. The TEM_{00} + TEM_{01*} equation is the only way to achieve approximate TEM_{FT} by existing optical means [72,73].

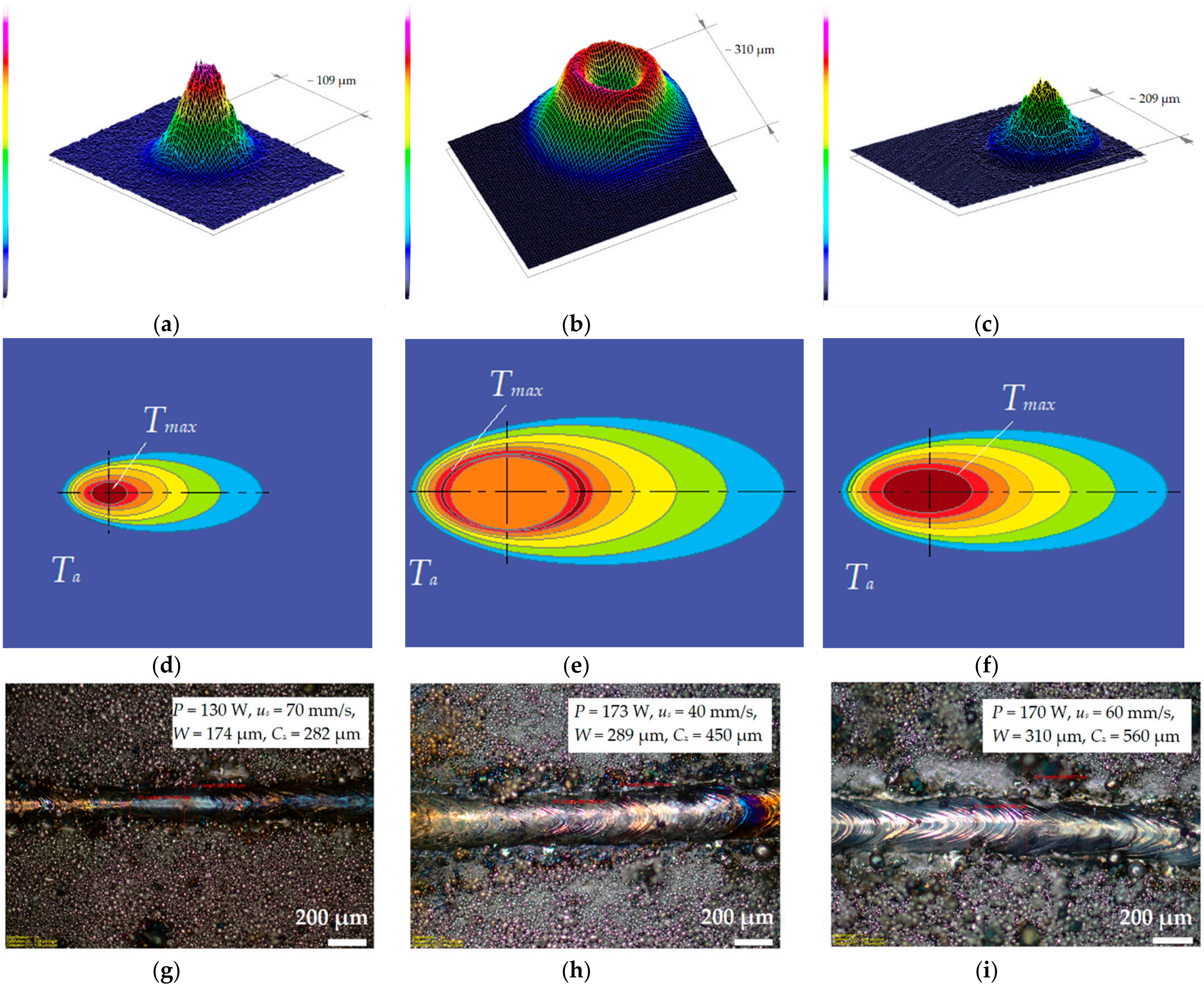

Figure 12. Laser beam profiles (objective control data achieved experimentally): (**a**) TEM_{00} (Gaussian); (**b**) TEM_{01*} (donut); (**c**) TEM_{FT} (flat-top); reconstruction of the temperature fields' features in the formed melt pools: (**d**) TEM_{00} (Gaussian); (**e**) TEM_{01*} (donut); (**f**) TEM_{FT} (flat-top); formed experimental tracks: (**g**) TEM_{00} (Gaussian); (**h**) TEM_{01*} (donut); (**i**) TEM_{FT} (flat-top), where W is a track's width, C_z is powder consolidation zone's width.

Comparing two radiation beams with different profiles is possible only with the different values for laser beam spot radii (Table 7). The same LPBF setup with a similar laser beam diameter provided technically and focused on a plane for all cases is practically used in the conditions of real production. Laser beam diameter corresponds to the main characteristics of the LPBF equipment (in our case, it is up to 100 µm) and cannot be changed quickly. The alternative laser beam profiles are experimentally achieved using a laser beam profiler and an expander and optically evaluated [60]. That was taken as a basis for theoretical evaluation of the dynamic factor to be closer to the common industrial conditions.

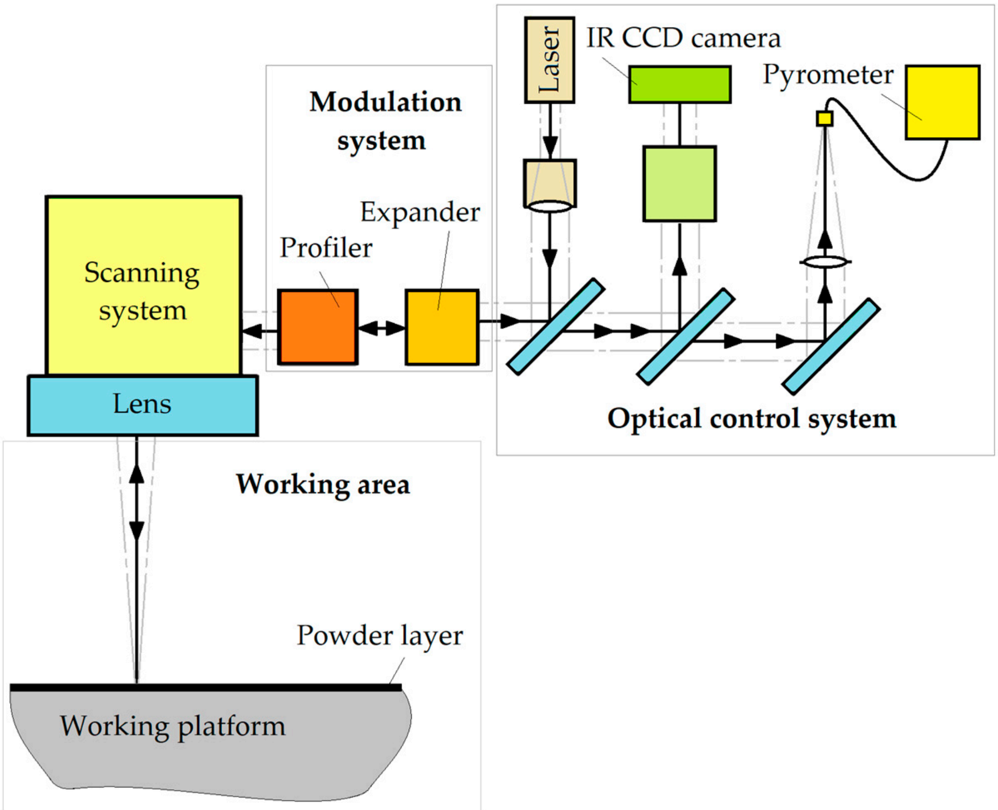

Figure 13. Modulation and optical control systems in-build into LPBF setup.

The average laser beam power distribution (E, J/m^2) will not be similar in these cases as it was previously evaluated and compared (Table 5). Still, the question is not in the energy density in the laser beam spot radii, but in the practically achievable profile that can be useful and implemented in standard or experimental LPBF equipment (Figure 13).

Practically, the achievable profile by mixing TEM_{00} and TEM_{01*} is far from the profile simulated based on Equation (2) due to the use available for market optical means. Moreover, as it was shown theoretically, the TEM_{FT} profile is not the one that corresponds the most to the technological tasks of LPBF of metallic powder with the high material thermal conductivity (λ).

5. Conclusions

Three radial laser beam profiles of the power density distribution (energy flux) were compared for laser powder bed fusion. The uniform cylindrical (flat-top) distribution (TEM_{01*} + TEM_{00} mode) was compared with the standard Laguerre–Gaussian law distribution TEM_{00} and the airy distribution of the first harmonic TEM_{01*} (TEM_{01} + TEM_{10} mode).

The TEM_{00} laser beam profile demonstrated the most effective result for a wide range of temperatures for thermos-activated processes such as laser powder bed fusion in the Péclet number range of 0–2.86, while the uniform cylindrical (flat-top) distribution is shown to be effective in a narrow temperature range. The inverse Gaussian (donut) laser beam distribution showed an interval result. With an increase in laser power, the transition from TEM_{00} to TEM_{01*} mode reduces the evaporation losses by more than 2.5 times, and it increases the absolute laser bandwidth when the relative bandwidth decreases by 24%.

The prospects of laser beam profiling for the purposes of increasing laser powder bed fusion productivity stay underestimated by the industry. However, they have a huge potential in the context of the switch to the sixth technological paradigm associated with Kondratieff's waves.

Author Contributions: Conceptualization, A.V.G. and S.N.G.; methodology, A.V.G.; software, A.S.G.; validation, A.S.M.; formal analysis, A.S.M. and T.V.T.; investigation, A.S.G. and T.V.T.; resources, T.V.T. and M.A.V.; data curation, A.A.O. and M.A.V.; writing—original draft preparation, A.A.O. and A.V.G.; writing—review and editing, A.V.G.; visualization, A.S.G., A.A.O. and A.V.G.; supervision, S.N.G.; project administration, S.N.G. and M.A.V.; funding acquisition, A.S.M. All authors have read and agreed to the published version of the manuscript.

Funding: This work was supported financially by the Ministry of Science and Higher Education of the Russian Federation (project No FSFS-2021-0003).

Institutional Review Board Statement: Not applicable.

Informed Consent Statement: Not applicable.

Data Availability Statement: Data are available in a publicly accessible repository.

Acknowledgments: The research was performed at the Department of High-Efficiency Processing Technologies of MSTU Stankin.

Conflicts of Interest: The authors declare no conflict of interest.

References

1. Lee, W.J.; Kim, E.A.; Woo, Y.J.; Park, I.; Yu, J.H.; Ha, T.; Choi, Y.S.; Lee, H.S. Effect of different WC particle shapes on laser-exposed microstructures during the directed energy deposition. *Powder Metall.* **2022**, *65*, 22–30. [CrossRef]
2. Ahsan, F.; Razmi, J.; Ladani, L. Process Parameter Optimization in Metal Laser-Based Powder Bed Fusion Using Image Processing and Statistical Analyses. *Metals* **2022**, *12*, 87. [CrossRef]
3. Gurin, V.D.; Kotoban, D.V.; Podrabinnik, P.A.; Zhirnov, I.V.; Peretyagin, P.Y.; Okunkova, A.A. Modeling of 3D technological fields and research of principal perspectives and limits in productivity improvement of selective laser melting. *Mech. Ind.* **2016**, *17*, 714. [CrossRef]
4. Khairallah, A.; Anderson, A.T.; Rubenchik, A.; King, W.E. Laser powder-bed fusion additive manufacturing: Physics of complex melt flow and formation mechanisms of pores, spatter, and denudation zones. *Acta Mater.* **2016**, *108*, 36–45. [CrossRef]
5. Sova, A.; Grigoriev, S.; Okunkova, A.; Smurov, I. Potential of cold gas dynamic spray as additive manufacturing technology. *Int. J. Adv. Manuf. Technol.* **2013**, *69*, 2269–2278. [CrossRef]
6. Sova, A.; Grigoriev, S.; Okunkova, A.; Sova, A.; Bertrand, P.; Smurov, I. Cold spraying: From process fundamentals towards advanced applications. *Surf. Coat. Technol.* **2015**, *268*, 77–84.
7. Monte, A.F.G.; Alves, G.A.; Marques, F.A.M. Thermal conductivity determination of erbium-doped crystals measured by spatially resolved confocal luminescence. *Appl. Opt.* **2018**, *57*, 7910–7914. [CrossRef]
8. Patel, S.; Reddy, P.; Kumar, A. A methodology to integrate melt pool convection with rapid solidification and undercooling kinetics in laser spot welding. *Int. J. Heat Mass Transf.* **2021**, *164*, 120575. [CrossRef]
9. Zhou, J.; Tsai, H.L. Modeling of transport phenomena in hybrid laser-MIG keyhole welding. *Int. J. Heat Mass Transf.* **2008**, *51*, 4353–4366. [CrossRef]
10. Doan, H.D.; Naoki, I.; Kazuyoshi, F. Laser processing by using fluidic laser beam shaper. *Int. J. Heat Mass Transf.* **2013**, *64*, 263–268. [CrossRef]
11. Litvin, I.A.; King, G.; Strauss, H. Beam shaping laser with controllable gain. *Appl. Phys. B-Lasers Opt.* **2017**, *123*, 1–5. [CrossRef]
12. Xia, X.P.; Cai, Z.B.; Yi, L. The splitted beam profile of laser beam in the interaction of intense lasers with overdense plasmas. *Laser Part. Beams* **2011**, *29*, 161–168. [CrossRef]
13. Gusarova, A.V.; Chumaevskii, A.V.; Osipovich, K.S.; Kalashnikov, K.N.; Kalashnikova, T.A. Regularities of Structural Changes after Friction Stir Processing in Materials Obtained by the Additive Method. *Nanosci. Technol.-Int. J.* **2020**, *11*, 195–205. [CrossRef]
14. Barro, Ó.; Arias-González, F.; Lusquiños, F.; Comesaña, R.; del Val, J.; Riveiro, A.; Badaoui, A.; Gómez-Baño, F.; Pou, J. Effect of Four Manufacturing Techniques (Casting, Laser Directed Energy Deposition, Milling and Selective Laser Melting) on Microstructural, Mechanical and Electrochemical Properties of Co-Cr Dental Alloys, Before and After PFM Firing Process. *Metals* **2020**, *10*, 1291. [CrossRef]
15. Sendino, S.; Gardon, M.; Lartategui, F.; Martinez, S.; Lamikiz, A. The Effect of the Laser Incidence Angle in the Surface of L-PBF Processed Parts. *Coatings* **2020**, *10*, 1024. [CrossRef]
16. Nalivaiko, A.Y.; Arnautov, A.N.; Zmanovsky, S.V.; Gromov, A.A. Al-Si-Cu and Al-Si-Cu-Ni alloys for additive manufacturing: Composition, morphology and physical characteristics of powders. *Mater. Res. Express* **2019**, *6*, 086536. [CrossRef]
17. Zavalov, Y.N.; Dubrov, A.V. Short Time Correlation Analysis of Melt Pool Behavior in Laser Metal Deposition Using Coaxial Optical Monitoring. *Sensors* **2021**, *21*, 8402. [CrossRef]
18. Chen, J.H.; Zhao, C.C.; Li, K.L.; Shen, Z.J.; Liu, W. Formability and Controlling of Cracks in Laser Powder Bed Fusion of Tungsten-5% Tantalum Carbide Alloys. *Chin. J. Lasers-Zhongguo Jiguang* **2021**, *48*, 1502006.
19. Alberti, E.A.; Bueno, B.M.P.; D'Oliveira, A.S.C.M. Additive manufacturing using plasma transferred arc. *Int. J. Adv. Manuf. Technol.* **2016**, *83*, 1861–1871. [CrossRef]

20. Kishore, V.; Ajinjeru, C.; Nycz, A.; Post, B.; Lindahl, J.; Kunc, V.; Duty, C. Infrared preheating to improve interlayer strength of big area additive manufacturing (BAAM) components. *Addit. Manuf.* **2017**, *14*, 7–12. [CrossRef]
21. Fateri, M.; Kaouk, A.; Cowley, A.; Siarov, S.; Palou, M.V.; Gonzalez, F.G.; Marchant, R.; Cristoforetti, S.; Sperl, M. Feasibility study on additive manufacturing of recyclable objects for space applications. *Addit. Manuf.* **2018**, *24*, 400–404. [CrossRef]
22. Sleiman, K.; Rettschlag, K.; Jaschke, P.; Capps, N.; Kinzel, E.C.; Overmeyer, L.; Kaierle, S. Material loss analysis in glass additive manufacturing by laser glass deposition. *J. Laser Appl.* **2021**, *33*, 042050. [CrossRef]
23. Żrodowski, Ł.; Wróblewski, R.; Choma, T.; Morończyk, B.; Ostrysz, M.; Leonowicz, M.; Łacisz, W.; Błyskun, P.; Wróbel, J.S.; Cieślak, G.; et al. Novel Cold Crucible Ultrasonic Atomization Powder Production Method for 3D Printing. *Materials* **2021**, *14*, 2541. [CrossRef] [PubMed]
24. Harkin, R.; Wu, H.; Nikam, S.; Quinn, J.; McFadden, S. Analysis of Spatter Removal by Sieving during a Powder-Bed Fusion Manufacturing Campaign in Grade 23 Titanium Alloy. *Metals* **2021**, *11*, 399. [CrossRef]
25. Zubko, M.; Loskot, J.; Świec, P.; Prusik, K.; Janikowski, Z. Analysis of Stainless Steel Waste Products Generated during Laser Cutting in Nitrogen Atmosphere. *Metals* **2020**, *10*, 1572. [CrossRef]
26. Metel, A.S.; Grigoriev, S.N.; Tarasova, T.V.; Melnik, Y.A.; Volosova, M.A.; Okunkova, A.A.; Podrabinnik, P.A.; Mustafaev, E.S. Surface Quality of Metal Parts Produced by Laser Powder Bed Fusion: Ion Polishing in Gas-Discharge Plasma Proposal. *Technologies* **2021**, *9*, 27. [CrossRef]
27. Okunkova, A.; Peretyagin, P.; Vladimirov, Y.; Volosova, M.; Torrecillas, R.; Fedorov, S.V. Laser-beam modulation to improve efficiency of selecting laser melting for metal powders. In Proceedings of the Conference on Laser Sources and Applications II, Laser Sources and Applications II, Brussels, Belgium, 14–17 April 2014; Mackenzie, J.I., Jelinkova, H., Taira, T., Ahmed, M.A., Eds.; SPIE-Int Soc Optical Engineering: Bellingham, WA, USA, 2014; Volume 9135, p. 913524.
28. Zhirnov, I.V.; Podrabinnik, P.A.; Okunkova, A.A.; Gusarov, A.V. Laser beam profiling: Experimental study of its influence on single-track formation by selective laser melting. *Mech. Ind.* **2015**, *16*, 709. [CrossRef]
29. Wang, S.D.; Zhang, X.; Zheng, Y.; Li, B.W.; Qin, H.T.; Li, Q. Similarity evaluation of 3D surface topography measurements. *Meas. Sci. Technol.* **2021**, *32*, 125003. [CrossRef]
30. Sagbas, B.; Gumus, B.E.; Kahraman, Y.; Dowling, D.P. Impact of print bed build location on the dimensional accuracy and surface quality of parts printed by multi jet fusion. *J. Manuf. Processes* **2021**, *70*, 290–299. [CrossRef]
31. Zakharov, O.V.; Brzhozovskii, B.M. Accuracy of centering during measurement by roundness gauges. *Meas. Tech.* **2006**, *49*, 1094–1097. [CrossRef]
32. Rezchikov, A.F.; Kochetkov, A.V.; Zakharov, O.V. Mathematical models for estimating the degree of influence of major factors on performance and accuracy of coordinate measuring machines. *MATEC Web Conf.* **2017**, *129*, 01054. [CrossRef]
33. Zakharov, O.V.; Balaev, A.F.; Kochetkov, A.V. Modeling Optimal Path of Touch Sensor of Coordinate Measuring Machine Based on Traveling Salesman Problem Solution. *Procedia Eng.* **2017**, *206*, 1458–1463. [CrossRef]
34. Wu, J.; Tao, K.; Miao, J.M. Production of centimeter-scale sub-wavelength nanopatterns by controlling the light path of adhesive photomasks. *J. Mater. Chem. C.* **2015**, *3*, 6796–6808. [CrossRef]
35. Sima, C.; Gates, J.C.; Rogers, H.L.; Mennea, P.L.; Holmes, C.; Zervas, M.N.; Smith, P.G.R. Phase controlled integrated interferometric single-sideband filter based on planar Bragg gratings implementing photonic Hilbert transform. *Opt. Lett.* **2013**, *38*, 727–729. [CrossRef]
36. Raciukaitis, G.; Stankevicius, E.; Gecys, P.; Gedvilas, M.; Bischoff, C.; Jager, E.; Umhofer, U.; Volklein, F. Laser Processing by Using Diffractive Optical Laser Beam Shaping Technique. *J. Laser Micro Nanoeng.* **2011**, *6*, 37–43. [CrossRef]
37. Nammi, S.; Vasa, N.J.; Balaganesan, G.; Gupta, S.; Mathur, A.C. Influence of pulsed Nd3+: YAG laser beam profile and wavelength on microscribing of copper and aluminum thin films. *J. Micro-Nanolithography Mems Moems* **2015**, *14*, 044503. [CrossRef]
38. Zhu, R.; Zhang, Y.K.; Lin, C.H.; Chen, Y. Residual stress distribution and surface geometry of medical Ti13Nb13Zr alloy treated by laser shock peening with flat-top laser beam. *Surf. Topogr.-Metrol. Prop.* **2020**, *8*, 045026. [CrossRef]
39. Yen, W.C.; Huang, C.T.; Liu, H.P.; Lee, L.P. A Nd:YAG laser with a flat-top beam profile and constant divergence. *Opt. Laser Technol.* **1997**, *29*, 57–61. [CrossRef]
40. Wu, T.N.; Wu, Z.P.; He, Y.C.; Zhu, Z.; Wang, L.X.; Yin, K. Femtosecond laser textured porous nanowire structured glass for enhanced thermal imaging. *Chin. Opt. Lett.* **2022**, *20*, 033801. [CrossRef]
41. Yin, K.; Wu, Z.P.; Wu, J.R.; Zhu, Z.; Zhang, F.; Duan, J.A. Solar-driven thermal-wind synergistic effect on laser-textured superhydrophilic copper foam architectures for ultrahigh efficient vapor generation. *Appl. Phys. Lett.* **2021**, *118*, 211905. [CrossRef]
42. Aleksandrova, M.; Nikolov, N.; Pandiev, I. Thermo-Stimulation of Charges by Peltier Element for Trap Analysis in Polymer Layers. *Int. J. Polym. Anal. Charact.* **2011**, *16*, 221–227. [CrossRef]
43. Gusarov, A.V. Radiative transfer, absorption, and reflection by metal powder beds in laser powder-bed processing. *J. Quant. Spectrosc. Radiat. Transf.* **2020**, *257*, 107366. [CrossRef]
44. Yu, H.; Hayashi, S.; Kakehi, K.; Kuo, Y.-L. Study of Formed Oxides in IN718 Alloy during the Fabrication by Selective Laser Melting and Electron Beam Melting. *Metals* **2019**, *9*, 19. [CrossRef]

45. Cao, Y.; Bai, P.; Liu, F.; Hou, X. Investigation on the Precipitates of IN718 Alloy Fabricated by Selective Laser Melting. *Metals* **2019**, *9*, 1128. [CrossRef]
46. Qin, Y.; Liu, J.; Chen, Y.; Wen, P.; Zheng, Y.; Tian, Y.; Voshage, M.; Schleifenbaum, J.H. Influence of Laser Energy Input and Shielding Gas Flow on Evaporation Fume during Laser Powder Bed Fusion of Zn Metal. *Materials* **2021**, *14*, 2677. [CrossRef]
47. Gokcekaya, O.; Ishimoto, T.; Todo, T.; Suganuma, R.; Fukushima, R.; Narushima, T.; Nakano, T. Effect of Scan Length on Densification and Crystallographic Texture Formation of Pure Chromium Fabricated by Laser Powder Bed Fusion. *Crystals* **2021**, *11*, 9. [CrossRef]
48. Grigoriev, S.N.; Metel, A.S.; Tarasova, T.V.; Filatova, A.A.; Sundukov, S.K.; Volosova, M.A.; Okunkova, A.A.; Melnik, Y.A.; Podrabinnik, P.A. Effect of Cavitation Erosion Wear, Vibration Tumbling, and Heat Treatment on Additively Manufactured Surface Quality and Properties. *Metals* **2020**, *10*, 1540. [CrossRef]
49. Wang, J.-H.; Ren, J.; Liu, W.; Wu, X.-Y.; Gao, M.-X.; Bai, P.-K. Effect of Selective Laser Melting Process Parameters on Microstructure and Properties of Co-Cr Alloy. *Materials* **2018**, *11*, 1546. [CrossRef]
50. Metel, A.S.; Stebulyanin, M.M.; Fedorov, S.V.; Okunkova, A.A. Power Density Distribution for Laser Additive Manufacturing (SLM): Potential, Fundamentals and Advanced Applications. *Technologies* **2019**, *7*, 5. [CrossRef]
51. Kopec, M.; Jóźwiak, S.; Kowalewski, Z.L. A Novel Microstructural Evolution Model for Growth of Ultra-Fine Al_2O_3 Oxides from SiO_2 Silica Ceramic Decomposition during Self-Propagated High-Temperature Synthesis. *Materials* **2020**, *13*, 2821. [CrossRef]
52. Bulina, N.V.; Makarova, S.V.; Baev, S.G.; Matvienko, A.A.; Gerasimov, K.B.; Logutenko, O.A.; Bystrov, V.S. A Study of Thermal Stability of Hydroxyapatite. *Minerals* **2021**, *11*, 1310. [CrossRef]
53. Kuzin, V.V.; Grigor'ev, S.N.; Volosova, M.A. Effect of a TiC Coating on the Stress-Strain State of a Plate of a High-Density Nitride Ceramic under Nonsteady Thermoelastic Conditions. *Refract. Ind. Ceram.* **2014**, *54*, 376–380. [CrossRef]
54. Volosova, M.A.; Grigor'ev, S.N.; Kuzin, V.V. Effect of Titanium Nitride Coating on Stress Structural Inhomogeneity in Oxide-Carbide Ceramic. Part 4. Action of Heat Flow. *Refract. Ind. Ceram.* **2015**, *56*, 91–96. [CrossRef]
55. Grigoriev, S.N.; Kozochkin, M.P.; Porvatov, A.N.; Volosova, M.A.; Okunkova, A.A. Electrical discharge machining of ceramic nanocomposites: Sublimation phenomena and adaptive control. *Heliyon* **2019**, *5*, e02629. [CrossRef]
56. Kimura, H.; Myung, W.N.; Kobayashi, S.; Suzuki, M.; Toda, K.; Yuine, T. Consolidation of Mechanically Alloyed Amorphous Conbzr Powder by HIP. *J. Jpn. Inst. Met.* **1992**, *56*, 833–841. [CrossRef]
57. Gusarov, A.V.; Grigoriev, S.N.; Volosova, M.A.; Melnik, Y.A.; Laskin, A.; Kotoban, D.V.; Okunkova, A.A. On productivity of laser additive manufacturing. *J. Mater. Process. Technol.* **2018**, *261*, 213–232. [CrossRef]
58. Ponomarev, S.V.; Bulanov, E.V.; Bulanova, V.O.; Divin, A.G. Minimization of Measurement Errors of the Coefficients of Heat Conductivity and Thermal Diffusivity of Thermal Insulating Materials by the Plane Pulsed Heat Source Method. *Meas. Tech.* **2019**, *61*, 1203–1208. [CrossRef]
59. Sova, A.; Okunkova, A.; Grigoriev, S.; Smurov, I. Velocity of the Particles Accelerated by a Cold Spray Micronozzle: Experimental Measurements and Numerical Simulation. *J. Therm. Spray Technol.* **2012**, *22*, 75–80. [CrossRef]
60. Gusarov, A.V.; Okun'kova, A.A.; Peretyagin, P.Y.; Zhirnov, I.V.; Podrabinnik, P.A. Means of Optical Diagnostics of Selective Laser Melting with Non-Gaussian Beams. *Meas. Tech.* **2015**, *58*, 872–877. [CrossRef]
61. Yadroitsev, I.; Bertrand, P.; Antonenkova, G.; Grigoriev, S.; Smurov, I. Use of track/layer morphology to develop functional parts by selectivelaser melting. *J. Laser Appl.* **2013**, *25*, 052003. [CrossRef]
62. Kotoban, D.; Grigoriev, S.; Okunkova, A.; Sova, A. Influence of a shape of single track on deposition efficiency of 316L stainless steel powder in cold spray. *Surf. Coat. Technol.* **2017**, *309*, 951–958. [CrossRef]
63. Doubenskaia, M.; Pavlov, M.; Grigoriev, S.; Tikhonova, E.; Smurov, I. Comprehensive Optical Monitoring of Selective Laser Melting. *J. Laser Micro Nanoeng.* **2012**, *7*, 236–243. [CrossRef]
64. Smurov, I.; Doubenskaia, M.; Grigoriev, S.; Nazarov, A. Optical Monitoring in Laser Cladding of Ti6Al4V. *J. Spray Tech.* **2012**, *21*, 1357–1362. [CrossRef]
65. Sova, A.; Grigoriev, S.; Okunkova, A.; Smurov, I. Cold spray deposition of 316L stainless steel coatings on aluminium surface with following laser post-treatment. *Surf. Coat. Technol.* **2013**, *235*, 283–289. [CrossRef]
66. Metel, A.; Tarasova, T.; Gutsaliuk, E.; Khmyrov, R.; Egorov, S.; Grigoriev, S. Possibilities of Additive Technologies for the Manufacturing of Tooling from Corrosion-Resistant Steels in Order to Protect Parts Surfaces from Thermochemical Treatment. *Metals* **2021**, *11*, 1551. [CrossRef]
67. Khmyrov, R.S.; Grigoriev, S.N.; Okunkova, A.A.; Gusarov, A.V. On the possibility of selective laser melting of quartz glass. *Phys. Procedia* **2014**, *56*, 345–356. [CrossRef]
68. Khmyrov, R.S.; Protasov, C.E.; Grigoriev, S.N.; Gusarov, A.V. Crack-free selective laser melting of silica glass: Single beads and monolayers on the substrate of the same material. *Int. J. Adv. Manuf. Technol.* **2016**, *85*, 1461–1469. [CrossRef]
69. Grigoriev, S.; Peretyagin, P.; Smirnov, A.; Solis, W.; Diaz, L.A.; Fernandez, A.; Torrecillas, R. Effect of graphene addition on the mechanical and electrical properties of Al2O3 -SiCw ceramics. *J. Eur. Ceram. Soc.* **2017**, *37*, 2473–2479. [CrossRef]
70. Li, E.L.; Wang, L.; Yu, A.B.; Zhou, Z.Y. A three-phase model for simulation of heat transfer and melt pool behaviour in laser powder bed fusion process. *Powder Technol.* **2021**, *381*, 298–312. [CrossRef]

71. Pelevin, I.A.; Ozherelkov, D.Y.; Chernyshikhin, S.V.; Nalivaiko, A.Y.; Gromov, A.A.; Chzhan, V.B.; Terekhin, E.A.; Tereshina, I.S. Selective laser melting of Nd-Fe-B: Single track study. *Mater. Lett.* **2022**, *315*, 131947. [CrossRef]
72. Gorshkov, B.G.; Danileiko, Y.K.; Nikolaev, V.N.; Sidorin, A.V. An Effect of Multiple Exposure in Laser Damage of Optical-Materials. *Kvantovaya Elektron.* **1983**, *10*, 640–643.
73. Baburin, N.V.; Galagan, B.I.; Danileiko, Y.K.; Il'ichev, N.N.; Masalov, A.V.; Molchanov, V.Y.; Chikov, V.A. Two-frequency mode-locked lasing in a monoblock diode-pumped Nd3+: GGG laser. *Quantum Electron.* **2001**, *31*, 303–304. [CrossRef]